

SOLUTION OF FREE-BOUNDARY PROBLEMS USING FINITE-ELEMENT/NEWTON METHODS AND LOCALLY REFINED GRIDS: APPLICATION TO ANALYSIS OF SOLIDIFICATION MICROSTRUCTURE

K. TSIVERIOTIS AND R. A. BROWN

Department of Chemical Engineering, Massachusetts Institute of Technology, Cambridge, MA 02139, U.S.A.

SUMMARY

A new method is presented for the solution of free-boundary problems using Lagrangian finite element approximations defined on locally refined grids. The formulation allows for direct transition from coarse to fine grids without introducing non-conforming basis functions. The calculation of elemental stiffness matrices and residual vectors are unaffected by changes in the refinement level, which are accounted for in the loading of elemental data to the global stiffness matrix and residual vector. This technique for local mesh refinement is combined with recently developed mapping methods and Newton's method to form an efficient algorithm for the solution of free-boundary problems, as demonstrated here by sample calculations of cellular interfacial microstructure during directional solidification of a binary alloy.

KEY WORDS Local mesh refinement Free boundary Finite element method Co-ordinate mapping Solidification

1. INTRODUCTION

Free-boundary problems involve both unknown field variables and unknown boundary shapes. In many cases the length scales and geometry of the free surface require more refined discretization along the surface than what is needed for resolution of field variables in the bulk of the domain. Examples of such cases come from a variety of physical problems such as viscous free-surface flows^{1,2} and microstructure formation during solidification.^{3–5} Many times for adequate resolution of this problem, more computational nodes are needed along the interface than in directions parallel to, but far from the interface. In the context of the finite element method, this requirement poses the problem of transition from a coarse to a fine grid. Various methods have been proposed for adaptive grid refinement that take into account the continuity and accuracy requirements of the finite element method.^{6–9} The purpose of this paper is not to review these methods, but rather to report on a discretization strategy not applied before in free-boundary problems. This discretization strategy combined with domain mapping techniques specially developed for free-boundary problems⁵ leads to a powerful methodology for treating efficiently a number of these problems.

The present study builds on our previous work,⁵ where a mapping was developed for the solution of free-boundary problems and applied to the calculation of highly deformed melt/solid interfaces that arise in the analysis of solidification microstructure formed during alloy solidification. This mapping transforms the solidification model from the physical domain to a computa-

tional domain where the unknown interface coincides with a co-ordinate line. The solidification model and the mapping equations are discretized by Galerkin finite element method applied on the transformed domain using a conforming grid of quadrilateral elements. The discrete non-linear equations are solved by Newton's method. While the combination of domain mapping and finite element/Newton methods provides a robust algorithm for solution of free-boundary problems at high boundary deformations, the discretization of the transformed domain used in Reference 5 was too simplistic to provide for consistent refinement for the field variables and the interface shape. These limitations are exemplified in Figures 1 and 2, where typical results are shown for the directional solidification of a binary alloy.

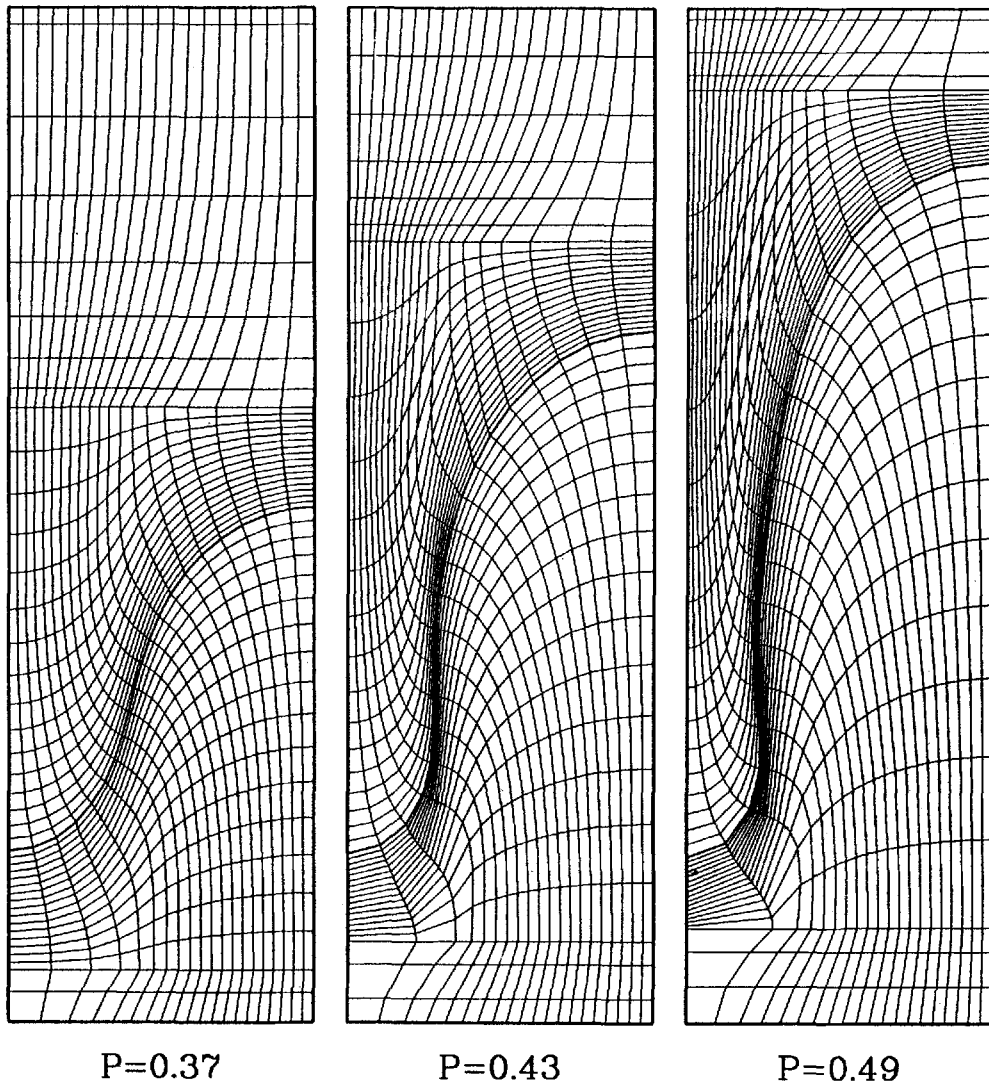


Figure 1. Transition to a deep solidification cell for increasing dimensionless solidification rate P . The computational grid is shown mapped back to the physical space. Here the interface is shown as a thicker co-ordinate line

In Figure 1 the evolution of a deep solidification cell is shown for increasing dimensionless solidification rate. As the cellular microstructure becomes deeper, the arclength at the interface increases, resulting in poor refinement of the interface shape and the unknown fields around the interface. It is clear that a significant increase of the discretization is needed locally around the interface. A less-deformed interface is shown in Figure 2 together with the corresponding concentration field. The interface shape involves length scales finer than the concentration field. The conforming discretization used in Figure 2 over-refines the approximation for the concentration field in the melt and solid, in order to achieve acceptable resolution at the interface. Again, local refinement is needed close to the interface.

In this paper we focus on the problem of local refinement around a free interface in the context of the finite element method. The goal of local refinement is to allow for a transition from a small number of elements away from the interface to large numbers of elements close to the interface. Continuity requirements for standard conforming finite elements¹⁰ allow elements to neighbour with only one element per side. Under this restriction, local refinement is only possible through the use of special transition layers of elements between the regions of low and high refinement. Two common examples⁶ are shown in Figures 3(a) and 3(b). In Figure 3(a), a layer of triangular elements is used to allow for the transition that doubles the number of elements. This method requires both the creation of an intermediate zone and the use of basis functions defined on triangular elements, in addition to the original quadrilateral bases. The second approach is shown in Figure 3(b) and involves only quadrilateral elements, but again requires the construction of a special intermediate zone between the regions with different refinement.

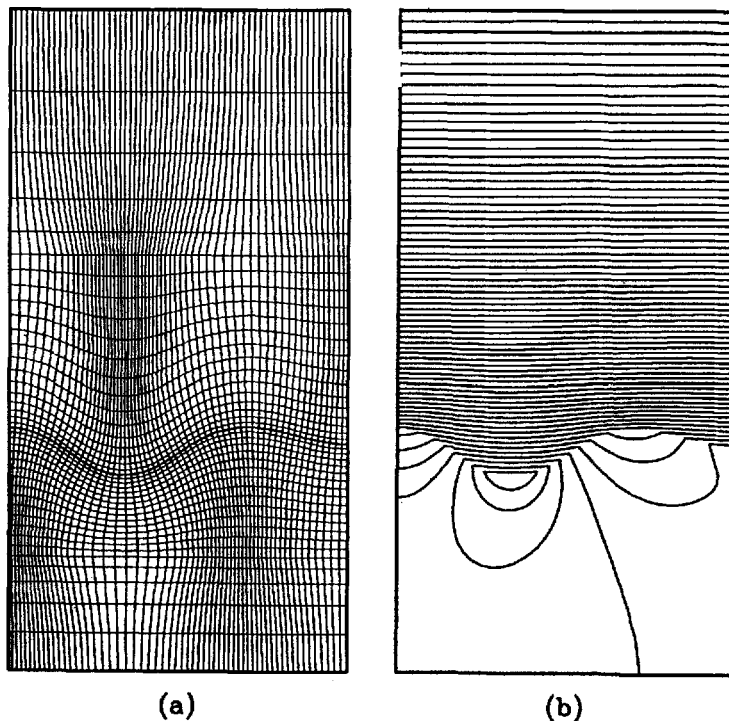


Figure 2. Shallow cellular structure arising in directional solidification. (a) computational grid (the interface is shown as a thicker co-ordinate line); (b) iso-concentration contours for concentration of solute

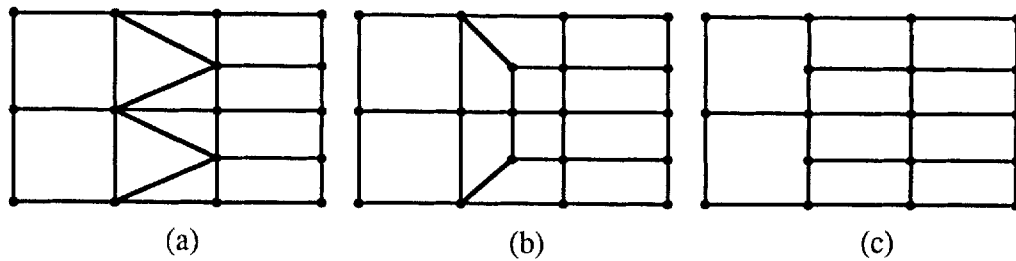


Figure 3. Transition from a coarse to a refined grid of quadrilaterals. (a) through a transition layer using triangles; (b) through a transition layer involving quadrilaterals only; (c) direct transition

Direct transition from a coarse to a fine grid, as shown in Figure 3(c), is a more attractive possibility, especially for automatic multilevel refinement of arbitrarily shaped parts of a computational domain. Nevertheless, this transition clearly violates the continuity requirements of the standard finite element methods. One approach to accommodate grids such as in Figure 3(c) is to use non-conforming elements, where approximations are allowed with simple discontinuities of derivatives of order $(m-1)$ or lower for boundary value problems of order $2m$.^{11,12} However, non-conforming elements are convergent approximations only under special conditions, e.g. fulfilment of the *patching test*,¹¹ and cannot be extended to arbitrary geometries and basis functions.^{12,13} In fact, we are not aware of any application of the classic patching test to the case of Figure 3(c). An alternative method is to use weak constraints that account for continuity in the context of hybrid finite element methods.¹⁴ This approach, while being general, introduces new contributions to the error estimates and requires considerable programming if it is to be incorporated to existing standard finite element codes.

The approach proposed in this study is the direct transition from coarse to fine discretizations, but without violating any requirements for conforming finite element approximations. This is achieved by specially treating the approximations at the transition in element number. This method has been used independently in solid mechanics by Gupta⁷ and recently in aerodynamics by Young *et al.*⁸ in the context of linear and trilinear finite elements, respectively. Here we present the method for general Lagrange finite element basis functions. Also, similar ideas have been used in the context of the finite volume method by Reggio *et al.*,¹⁵ where nodes on the transition boundary are treated so that the conservation principles involved in the finite volume method are not violated.

The proposed method for local refinement is applied to the calculation of microstructure from a model of directional solidification; the solutal model and mapping equations for directional solidification of a binary alloy are presented in Section 2. The local refinement method is presented in Section 3 and its advantages and limitations are discussed. Sample results for directional solidification obtained using local refinement are presented in Section 4 and are compared with calculations without local refinement.

2. THE SOLUTAL/MAPPING EQUATIONS

The solutal model used for directional solidification of a binary alloy together with the mapping equations used to treat the unknown shape of the domain are described in detail in Reference 5. Here we briefly describe the physical system and summarize the equations and boundary conditions.

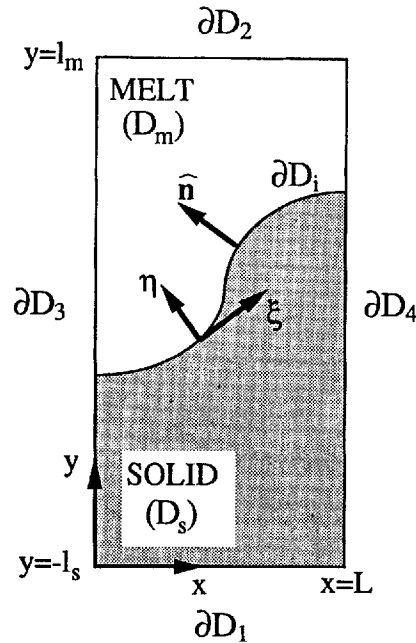


Figure 4. The two-dimensional domain of thin-film directional solidification

A configuration of the physical system is shown in Figure 4, where a thin film of a binary alloy is transported with constant velocity through an externally imposed temperature gradient. As the melt solidifies, solute is rejected from the solid to the melt resulting in a high solute concentration in a melt layer adjacent to the interface. Higher solute concentrations lead to higher melting points and if the melting point in the solute-enriched layer is higher than the temperature, then irregular freezing occurs leading to a non-planar melt/solid interface. This instability of the planar solidification front was described originally by Tiller *et al.*¹⁶ and the relevant linear stability analysis was performed later by Mullins and Sekerka.¹⁷ Our goal is the study of the non-planar interface morphologies that evolve after the instability of the planar interface.

The solutal model is a good continuum approximation of the physics of the formation of interfacial microstructure in directional solidification. Here the latent heat of solidification is assumed negligible, the thermal diffusivities in the melt and the solid are assumed equal, and convection of heat in melt and solid is neglected. Under these assumptions, the thermal field is decoupled from the interface position and is considered to have constant linear profile, $T=1+Gy$. This equation and the others appearing below are written in dimensionless variables, where lengths are scaled with a characteristic length L_0 , time with the diffusion time $\tau_d=L_0^2/\mathcal{D}_m$, temperature with the melting temperature of pure material T_m^0 , and concentration with the bulk concentration of the alloy c_∞ . Quantities referring to the melt and solid phases are denoted by the subscripts m and s, respectively. The unknowns in the solutal model are the solute concentration in the solid and the melt and the interface shape.

The solute conservation equations in the melt and the solid are

$$\frac{\partial c_m}{\partial t} = \nabla^2 c_m + P(\hat{\mathbf{e}}_y \cdot \nabla c_m), \quad (1)$$

$$\frac{\partial c_s}{\partial t} = R_m \nabla^2 c_s + P(\hat{\mathbf{e}}_y \cdot \nabla c_s) \quad (2)$$

where $R_m \equiv \mathcal{D}_s/\mathcal{D}_m$ is the ratio of solutal diffusivity in the solid to the value in the melt, and $P \equiv L_0 V/\mathcal{D}_m$ is the solutal Peclet number expressing the dimensionless solidification rate in the y -direction. The solute balance across the interface is

$$\hat{\mathbf{n}} \cdot \nabla c_m - R_m \hat{\mathbf{n}} \cdot \nabla c_s = (c_m - c_s) \left(-P \hat{\mathbf{e}}_y \cdot \hat{\mathbf{n}} + \left[\frac{1}{|\nabla F|} \frac{\partial F}{\partial t} \right]_{F=0} \right) \quad \text{at } \partial D_1, \quad (3)$$

where $F(x, y, t) = 0$ is the parametrization of the interface and $\hat{\mathbf{n}} \equiv [\nabla F/|\nabla F|]_{F=0}$ is the normal vector to the interface. Local thermodynamic equilibrium is assumed at the interface in terms of a partition coefficient k ,

$$c_s = k c_m \quad \text{at } \partial D_1, \quad (4)$$

and the Gibbs–Thomson equation is used to account for the effects of the solute concentration and the interface curvature on the melting point

$$T = 1 + Gy = 1 + m c_m + 2\mathcal{H}\Gamma \quad \text{at } \partial D_1, \quad (5)$$

where m is the dimensionless slope of the liquidus line of the phase diagram, $2\mathcal{H} \equiv -\nabla_s \cdot \hat{\mathbf{n}}$ is the interface curvature and $\Gamma \equiv \tilde{\Gamma}/L_0$ is the dimensionless capillary constant. The boundary conditions for the solute concentration at the far field are

$$\hat{\mathbf{e}}_y \cdot \nabla c_m = P(1 - c_m) \quad \text{at } \partial D_2, \quad (6)$$

$$\hat{\mathbf{e}}_y \cdot \nabla c_s = 0 \quad \text{at } \partial D_1. \quad (7)$$

Reflective boundary conditions are assumed at the domain sides:

$$\hat{\mathbf{e}}_x \cdot \nabla c_m = 0, \quad \hat{\mathbf{e}}_x \cdot \nabla c_s = 0 \quad \text{at } \partial D_3, \partial D_4, \quad (8)$$

$$\phi = 0 \quad \text{at } \partial D_3, \partial D_4, \quad (9)$$

where ϕ is the angle formed by the unit vector tangent to the interface and pointing in the direction of increasing interfacial arclength and the unit vector $\hat{\mathbf{e}}_x$.

The equations (1)–(9) are solved simultaneously with the mapping equations that extend to both the solid and melt phases and transform the regions with the free boundary in physical space to a fixed domain in co-ordinates (ξ, η) . The mapping equations developed in Reference 5 are

$$\mathbf{V} \cdot (\mathbf{a} \cdot \nabla \eta) = f(\eta), \quad (10)$$

$$\mathbf{V} \cdot \left[\sqrt{\left(\frac{x_\xi^2 + y_\xi^2}{x_\eta^2 + y_\eta^2} \right) + \varepsilon(\eta)} \right] \nabla \xi = 0, \quad (11)$$

where

$$\mathbf{a} = \begin{pmatrix} 1 & 0 \\ 0 & a(\eta) \end{pmatrix}, \quad a(\eta) \gg 1.$$

Equation (10) is the heat equation that distributes the ξ -co-ordinate lines ($\eta = \text{constant}$), so that they follow the interface shape as close as possible. Equation (10) results in η -co-ordinate lines that pass through the ξ -co-ordinate lines as smoothly and orthogonally as possible. The interface always coincides with the ξ -axis and the ξ co-ordinate is distributed uniformly with respect to

arclength along this axis, according to

$$\eta = 0, \quad \xi = \frac{\int_0^\xi \sqrt{(x_{\xi'}^2 + y_{\xi'}^2)} d\xi'}{\int_0^1 \sqrt{(x_{\xi'}^2 + y_{\xi'}^2)} d\xi'}, \quad \text{at } \partial D_1. \tag{12}$$

Orthogonality conditions are assumed on the other domain boundaries:

$$\hat{e}_y \cdot \nabla \xi = 0, \quad \eta = 1, -1 \quad \text{at } \partial D_1, \partial D_2, \tag{13}$$

$$\hat{e}_x \cdot \nabla \eta = 0, \quad \xi = 0, 1 \quad \text{at } \partial D_3, \partial D_4. \tag{14}$$

The mapping of the physical to the computational domain is improved by decoupling the mapping of the domain around the interface, $\eta_1 \leq \eta \leq \eta_2$, from that of the far-field domain, $-1 \leq \eta \leq \eta_1$ and $\eta_2 \leq \eta \leq 1$, where $\eta = \eta_1$ and $\eta = \eta_2$ are two transformed co-ordinate lines above and below the interface, as shown in Figures 1 and 7. The mapping equations in the inner region of the domain, $\eta_1 \leq \eta \leq \eta_2$, are solved independently with boundary conditions

$$\hat{e}_y \cdot \nabla \xi = 0 \quad \text{at } \eta = \eta_1, \eta_2.$$

The mapping of the far field is coupled to the mapping of the inner region by using the results from the inner region along the axes $\eta = \eta_1$ and $\eta = \eta_2$ as essential conditions for the solution of the mapping equations in the regions $-1 \leq \eta \leq \eta_1$ and $\eta_2 \leq \eta \leq 1$, respectively. In addition, the ξ -co-ordinate lines are stretched in the outer domain, as shown in Figures 1 and 2, by changing the scaling of the tensor \mathbf{a} in equation (10) to

$$\mathbf{a} = \begin{pmatrix} b & 0 \\ 0 & a(\eta) \end{pmatrix}, \quad a(\eta) \ll b.$$

The Galerkin finite element is used to discretize the boundary value problem given by equations (1)–(14) using bilinear approximations for the mapping unknowns (x, y) and biquadratic for the concentration field defined over the transformed domain $0 < \xi < 1$ and $-1 < \eta < 1$; this weak formulation is described in detail in Reference 5 and is not repeated here. It will be apparent in the next section that local refinement does not affect the weak formulation derived in Reference 5.

3. LOCAL REFINEMENT USING ONE-TO-TWO ELEMENT TRANSITIONS

In this section we develop a Lagrangian finite element approximation to an arbitrary field variable $u(x, y)$ using locally refined quadrilateral meshes. We consider the collection of elements shown in Figure 5, where a transition from element e_3 to elements e_1 and e_2 is shown. We refer to a boundary of such an one-to-two element transition as a *transition boundary*. The characteristic of a transition boundary is that it contains two sets of nodes. The first set of nodes are boundary nodes of the coarse element lying on one side of the transition boundary and the second set consists of the boundary nodes of the two refined elements lying on the other side of the transition boundary. We refer to the first set of nodes as *regular nodes* and to the second set as *pseudonodes*. The discussion that follows assumes that finite element approximations in each element are constructed using p -order Lagrangian basis functions defined at nodes in each element. These nodes are shown schematically in Figure 5 for bilinear approximations.

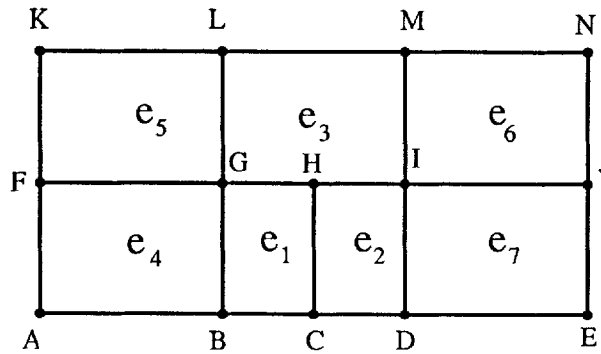


Figure 5. Example of local refinement through element splitting

Let $\{n_1^i, n_2^i, n_3^i\}, i = 1, \dots, m$, be the nodes of the elements e_1, e_2 and e_3 along the boundaries GH, HI and GI , respectively. Then $\{n_1^i, n_2^i\}$ are the pseudonodes and $\{n_3^i\}$ are the regular nodes of the transition boundary GI . Also let $\{\psi_j^n\}$ be the *elemental basis function* corresponding to node n and defined over element e_j . Each basis function ψ_j^n is non-zero at node n and is zero at all other nodes of elements e_j .

The problem of continuity across the transition boundary comes from the fact that the elemental basis functions $\{\psi_3^{n_3^i}\}$ defined over the coarse element and corresponding to the regular nodes cannot be extended to the other side of the transition boundary to the elemental basis functions $\{\psi_1^{n_1^i}\}$ and $\{\psi_2^{n_2^i}\}$, which correspond to the pseudonodes. This discontinuity results in two limitations: (i) the continuity of the solution is not guaranteed for any arbitrary set of nodal values of the unknown fields and (ii) *global basis functions* Φ cannot be formed at the transition boundaries by simply patching together elemental bases functions that have the continuity appropriate for second-order elliptic problems, i.e. $\Phi(\mathbf{x}) \in \mathcal{H}^1(\Omega) = \{\Phi, \int_{\Omega} [\Phi^2 + |\nabla\Phi|^2] d\Omega < \infty\}$.

This problem is alleviated by enforcing the continuity of the solution across the transition boundary GI by introducing essential conditions for the values of the unknowns at the pseudonodes,

$$u_{n_1^i} = \sum_{j=1}^m w_{n_3^i}^{n_1^j} u_{n_3^j}, \quad i = 1, \dots, m, \tag{15}$$

$$u_{n_2^i} = \sum_{j=1}^m w_{n_3^i}^{n_2^j} u_{n_3^j}, \quad i = 1, \dots, m, \tag{16}$$

where u_n is the value of the unknown field u at the node n and the weightings w_n^l are given by the values at the pseudonodes l of the shape functions corresponding to the regular nodes n , i.e.

$$w_{n_3^i}^{n_1^j} = \psi_3^{n_3^i}(n_1^j), \quad w_{n_3^i}^{n_2^j} = \psi_3^{n_3^i}(n_2^j), \quad i = 1, \dots, m, \quad j = 1, \dots, m. \tag{17}$$

The conditions (15) and (16) remove the pseudonodes from the finite element formulation leaving only the regular nodes along the transition boundaries. The latter set of nodes is introduced into the finite element formulation by defining new global basis functions $\{\Phi_{n_3^i}\} \subset H^1(\Omega)$ on the nodes $\{n_3^i\}$. This is done by patching the elemental basis functions corresponding to a regular node of a transition boundary together with a weighted combination of the elemental basis functions corresponding to the pseudonodes of the transition boundary. The weighting coefficients used are the same ones used in the continuity constraints; see equation (17). For the example in Figure 5,

the basis functions of the regular nodes $\{n_3^i\}$ are

$$\Phi_{n_3^i} = \sum_{j=1}^m w_{n_3^i}^{n_j^i} \psi_1^{n_j^i} + \sum_{j=1}^m w_{n_3^i}^{n_j^i} \psi_2^{n_j^i} + \psi_3^{n_3^i}, \quad i = 2, m - 1, \tag{18}$$

$$\Phi_{n_3^i} = \sum_{j=1}^m w_{n_3^i}^{n_j^i} \psi_1^{n_j^i} + \sum_{j=1}^m w_{n_3^i}^{n_j^i} \psi_2^{n_j^i} + \psi_3^{n_3^i} + \psi_4^{n_3^i} + \psi_5^{n_3^i}, \tag{19}$$

$$\Phi_{n_3^m} = \sum_{j=1}^m w_{n_3^m}^{n_j^m} \psi_1^{n_j^m} + \sum_{j=1}^m w_{n_3^m}^{n_j^m} \psi_2^{n_j^m} + \psi_3^{n_3^m} + \psi_6^{n_3^m} + \psi_7^{n_3^m}, \tag{20}$$

where we assumed that the nodes n_3^1 and n_3^m coincide with the points G and I , respectively. The definitions (18)–(20) of the global basis functions $\{\Phi_{n_3^i}\}$ guarantees continuity and local support.

Calculation of the various terms of the weak formulation of the Galerkin finite element method involves the calculation of integrals of the form

$$I_i = \int_{\Omega} f \Phi_i \, dA \quad \text{and} \quad I'_{i,x_j} = \int g \frac{\partial \Phi_i}{\partial x_j}, \quad j = 1, 2, \tag{21}$$

where $\{x_j\}$ are the components of the position vector. In standard finite elements, these integrals are estimated as an assembly of elemental integrals involving elemental basis functions. This element-by-element assembly can be extended to integrals involving basis functions of the form, equations (18)–(20). Using equations (18)–(20) to evaluate the integral $I_{n_3^i}$ for a regular node n_3^i gives

$$I_{n_3^i} = \sum_{j=1}^m w_{n_3^i}^{n_j^i} \hat{I}_1^{n_j^i} + \sum_{j=1}^m w_{n_3^i}^{n_j^i} \hat{I}_2^{n_j^i} + \hat{I}_3^{n_3^i}, \quad i = 2, m - 1, \tag{22}$$

$$I_{n_3^i} = \sum_{j=1}^m w_{n_3^i}^{n_j^i} \hat{I}_1^{n_j^i} + \sum_{j=1}^m w_{n_3^i}^{n_j^i} \hat{I}_2^{n_j^i} + \hat{I}_3^{n_3^i} + \hat{I}_4^{n_3^i} + \hat{I}_5^{n_3^i}, \tag{23}$$

$$I_{n_3^m} = \sum_{j=1}^m w_{n_3^m}^{n_j^m} \hat{I}_1^{n_j^m} + \sum_{j=1}^m w_{n_3^m}^{n_j^m} \hat{I}_2^{n_j^m} + \hat{I}_3^{n_3^m} + \hat{I}_6^{n_3^m} + \hat{I}_7^{n_3^m}, \tag{24}$$

where

$$\hat{I}_e^n \equiv \int_e f \psi_e^n \, dA. \tag{25}$$

Similar expressions are obtained for I'_{i,x_j} .

Based on these expressions, the proposed formulation is implemented in existing Lagrangian finite element codes with minimal changes. In particular, the formation of elemental stiffness matrices and residuals is not affected at all. Changes are needed only at the loading of the elemental data to the global stiffness matrix and residual. This involves two steps for each pseudonode n : (i) the interpolation constraint step, where the residuals and stiffness entries corresponding to pseudonode n are replaced by the constraints (15) and (16) and (ii) the redistribution step, where the elemental data corresponding to the pseudonode n are weighted, as shown in the summation terms in equations (22)–(24) and loaded to the global entries corresponding to the regular nodes of the transition boundary.

The order of approximation over e_1 and e_2 is affected by the constraints (15) and (16). After equations (15) and (16) are applied, the elements e_1 and e_2 are not regular but rather form a compound element which we refer to as $e_{1,2}$. The basis functions of the compound element are those of e_1 and e_2 , except at the transition boundary GI , where the basis functions are defined on

the nodes n_3^i , $i=1, \dots, m$, as dictated by equations (18)–(20). If the accuracy along a side of a regular element is $\mathcal{O}(h^n)$, the accuracy along the transition boundary of the compound element $e_{1,2}$ is only $\mathcal{O}(h^n)$ instead of $\mathcal{O}((h/2)^n)$, as happens with the side BD of the compound element. In other words, the accuracy of approximation in the area $e_1 \cup e_2$ is between that of element e_3 and the regular elements e_1 and e_2 alone. Of course, this reduced accuracy is restricted only to the finer elements adjacent to the transition boundary and does not extend to the refined regular elements adjacent to the side BD of $e_{1,2}$.

The refinement procedure clearly allows the direct transition from a number of elements to twice as many. There are numerous possibilities for initializing and updating the numbering and the data structure of this refinement transition, depending on the solution method for the resulting non-linear algebraic equations and the machine architecture. According to this approach, a uniform collection of elements is constructed and then elements in regions where refinement is needed are split repeatedly until the desired resolution is achieved. Similarly, elements in regions where a coarser grid is needed are coalesced from two to one. Both splitting and coalescence of elements are automatically performed so that only one-to-two element transitions are allowed. The numbering of elements and nodes remains arbitrary during grid generation and the next available integer is given to every new element, node, or unknown. The relationships between refined elements and their coarser ancestors are not stored as in other approaches.⁸

A pathological case may arise during automatic multilevel local refinement if arbitrary transitions from one to two elements are allowed. This problem is exemplified in Figure 6 for bilinear elements where the element e_1 contains pseudonode H and is split horizontally into elements \hat{e}_1 and e_4 , while element e_2 is not split. Following the method described above, a portion of the elemental data from \hat{e}_1 and e_4 corresponding to the pseudonode O must be loaded to node H , as dictated by equations (22)–(24). However, node H is also a pseudonode related to the transition boundary GI and, thus, all elemental contributions to this node have to be distributed to the regular nodes G and I , as described by equations (22)–(24). This results in transferring data from element e_4 to nodes G and I of element e_3 , which is not adjacent to e_4 . The situation becomes more complex if element e_4 is required to be split horizontally. Implementation of such

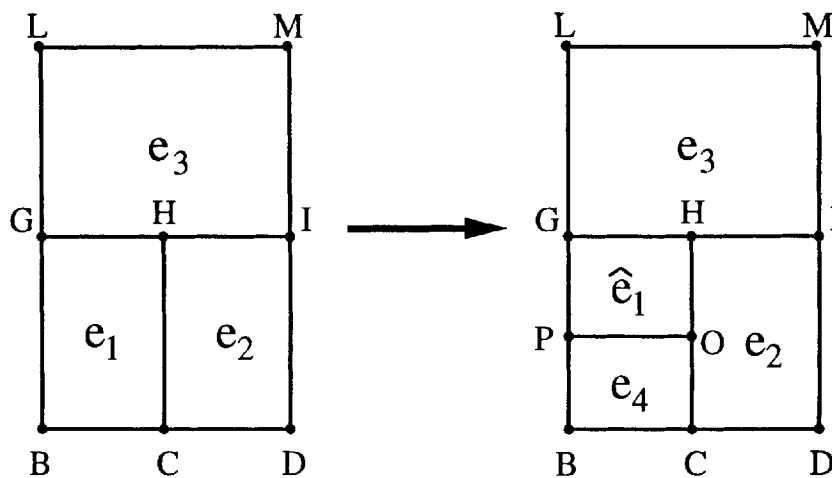


Figure 6. Splitting of element that already contains pseudonodes on the sides to be split. Such transitions while possible in principle are not allowed in this approach

transitions in mesh refinement requires very sophisticated data structures that are not justified by the additional improvement in refinement derived by introducing these element configurations. In the implementation applied here, such transitions are not allowed; we require for an element to be split, that all the nodes are regular along the two sides of the element involved in the subdivision.

An example of automatic local refinement is shown in Figure 7 for a rectangular domain with $0 \leq x \leq 2$ and $0 \leq y \leq 1$. Here refinement is done in levels; at each level a group of elements is split horizontally or vertically. In Figure 7, four levels of refinement, two vertical and two horizontal, have been applied in the square area defined by $0.2 \leq x \leq 0.7$ and $0.2 \leq y \leq 0.7$. Similarly, one vertical and one horizontal refinement levels have been applied to the circular area $(x-2)^2 + (y-1)^2 \leq 0.4$; the same refinement has been repeated in the area with $(x-2)^2 + (y-1)^2 \leq 0.8$, achieving a spatially graded refinement towards the upper right corner of this domain.

In the calculations of solidification microstructure described in this paper, local refinement is applied to both the bilinear and biquadratic elemental representations used for the mapping unknowns (x, y) and concentration field, respectively. Newton's method is used for the solution of the non-linear algebraic equations resulting from the finite element discretization⁵ of the solutal/mapping equations. The linear systems appearing at each Newton iteration are solved by direct LU factorization of the stiffness matrix using frontal storage techniques designed for a vector serial computer. The computational work required for the LU factorization is the dominant computational expense for these calculations and scales as W^2N , where W is the bandwidth of the Jacobian matrix and N is the number of the unknowns. To achieve optimal performance the bandwidth of the Jacobian matrix must be minimized; this amounts to addressing the elements in the frontal solver in a suitable order, which is found by implementing standard bandwidth minimization methods.¹⁸ In the application described here, the discretization is uniformly refined in the lateral direction (ξ) and the optimal numbering is intuitively found to be the one that scans all consecutive elements in the η -direction before scanning their neighbours in the lateral ξ -direction. In fact, this numbering results in the same bandwidth for the stiffness matrix as the one that corresponds to the original unrefined grid. Because the bandwidth remains unaffected by the local refinement, the computational work involved in these calculations is proportional only to the number of degrees of freedoms introduced by each level of discretization.

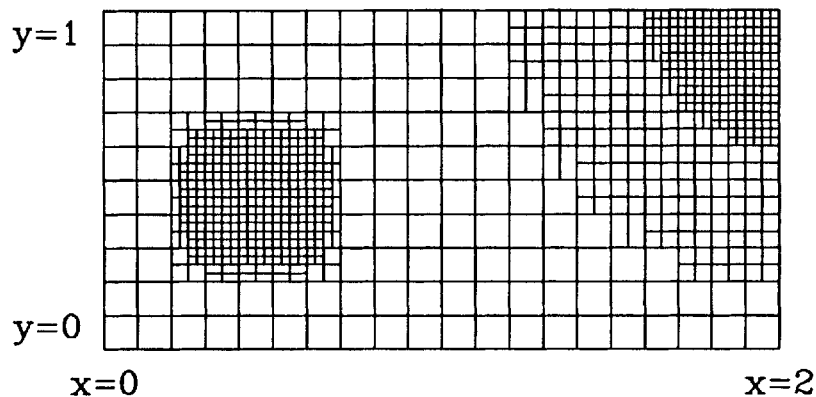


Figure 7. Example of automatic multilevel local refinement. The construction of the mesh is described in the text

4. RESULTS

The efficiency of the proposed method for local refinement is demonstrated here for solution of the solutal model and mapping equations for development of cellular interface morphologies in directional solidification. It is well known^{4,5} that the steady-state solutions of this problem present a very rich bifurcation structure. Here our goal is not to explore this non-linear solution structure, but rather to use some of the steady states as examples for local refinement. The system considered is the solidification of Pb-Sb alloy with material properties and operating parameters identical to those used in Reference 5. In Reference 5, we have calculated the structure of the primary solutions bifurcating from the planar interface state for increasing dimensionless solidification rate P . In those computations the lateral size of the domain was taken equal to the critical wavelength λ_c corresponding at the onset of the instability of the planar state. Here we follow a similar approach as we reconsider the two cases of Figures 1 and 2 involving deep and shallow solidification cells, respectively.

Mesh refinement is performed in layers symmetric in the melt and solid around the interface and uniform in the lateral direction. Every level of refinement is characterized by an integer n , meaning that the elements in a layer n -element thick above and below the interface are vertically split so that the number of elements along the interface is doubled. Thus, a refined grid is characterized by the original uniform discretization together with a set of integers n_i , $i = 1, \dots, m$ indicating the m consecutive levels of refinement, each defining a $2n_i$ -element thick region. For example the grid shown in Figure 8(b) is a (20×55) grid with refinement $(10, 5)$.

The first case considered is the case of a deep cell of Figure 1 corresponding to the primary bifurcation family with wavelength $\lambda_c/4$, which also is shown in the bifurcation diagram in Figure 13 of Reference 5. The calculations presented here are for a domain with length equal to $\lambda_c/8$. In these calculations, we use uniform grids $G1 = (20, 55)$, $G2 = (40, 55)$ and $G3 = (80, 55)$, and locally refined grids derive from $G1$ and $G2$. The performance of these discretizations for computing y -position of the bottom of the interfacial cell is compared relative to the more accurate value obtained using a finer uniform grid $G4 = (160, 55)$. The results are summarized in Table I where it is apparent that the accuracy of the calculated position of the bottom of the interface is affected by the total number of degrees-of-freedom representing the interface shape, rather than by the total number of degrees-of-freedom. For example, the grids $G1a$ and $G2$ have the same accuracy and same number of nodes on the interface, while the first grid involves only half the unknowns of the second. Also, grid, $G1e$ achieves an order-of-magnitude higher accuracy

Table I. Results for deep cell computed with various refinement

Grid	Original (x, y) discretization	Local refinement	Degrees of freedom	Elements on interface	Relative error
G1	20×55	0	5803	20	5.5×10^{-2}
G1a	20×55	5	6883	40	1.4×10^{-2}
G1b	20×55	5, 5	8643	80	3.8×10^{-3}
G1c	20×55	10	7883	40	1.4×10^{-2}
G1d	20×55	10, 10	11 643	80	3.1×10^{-3}
G1e	20×55	10, 5	10 043	80	3.2×10^{-3}
G2	40×55	0	11 383	40	1.3×10^{-2}
G2a	40×55	5	13 543	80	2.7×10^{-3}
G2b	40×55	10	15 543	80	2.7×10^{-3}
G3	80×55	0	22 543	80	2.7×10^{-3}

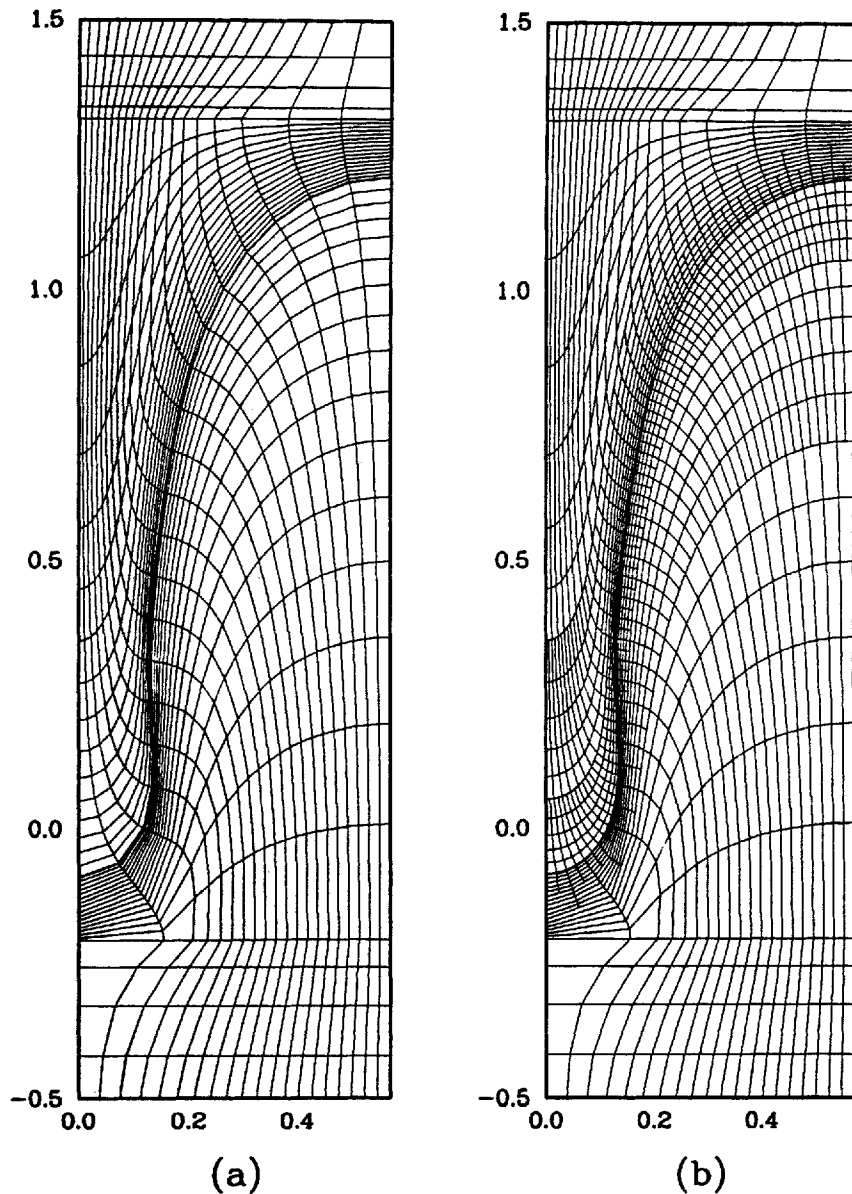


Figure 8. Uniform and locally refined mesh for a deep cell at $P=0.49$. Here the domain is shown truncated for $-0.5 \leq y \leq 1.5$, while the full computational domain used is $-1.5 \leq y \leq 3.5$. The discretizations of (a) and (b) correspond to the grids G_1 and G_6 of Table I, respectively. The interface is shown as a thicker co-ordinate line

than the uniform grid G_2 , while using slightly fewer unknowns than in G_2 . The interface shape and the corresponding grids in the physical space are shown in Figures 8 and 9 for some of the discretizations described in Table I. The improvement of the approximation of the interface shape is apparent.

The second case considered is the example of a shallow interface shape shown in Figure 2. This steady state belongs to a secondary bifurcating branch emanating from the primary solution with

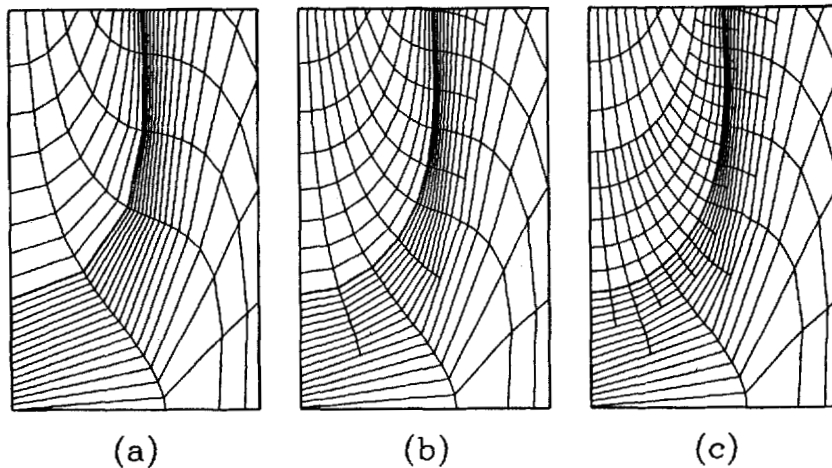


Figure 9. Detail of the representation for the bottom of the deep cell. The discretizations used are (a) G1, (b) G4c, and (c) G6c of Table I. The interface is shown as a thicker co-ordinate line

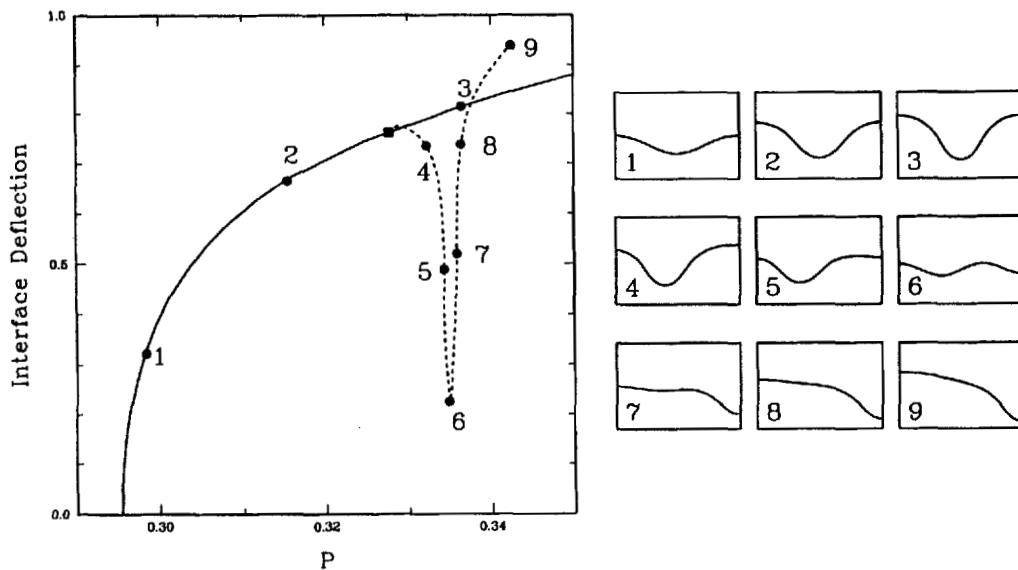


Figure 10. Bifurcation diagram showing the amplitudes of the primary solution with wavelength $\lambda_c/2$ and the secondary solution as a function of P in a domain with length $\lambda_c/2$. Shapes of the interface are also shown. These results have been obtained using the discretization G6 of Table II

wavelength $\lambda_c/2$, as shown in Figure 10. We study this secondary solution because the interface shape changes rapidly as P is increased, making local refinement critical for obtaining the correct interface shape at a given value of the growth rate. The computational domain used is $\lambda_c/2$. The various refinements used are described in Table II and the results are depicted as bifurcation branches in Figure 11. Here the approximation error can be seen as the distance of the various solution branches from the solution branch that corresponds to the finest grid G6. From Figure 11, it is clear that refinement around the interface rather than the total number of un-

Table II. Grids used in the calculation of the shallow cell

Grid	Original (x, y) x-discretization	Local refinement	Degrees of freedom	Elements on interface
G4	15 × 40	0	3223	15
G4a	15 × 40	5	4033	30
G4b	15 × 40	8, 5	6103	60
G5	30 × 40	0	6283	30
G5a	30 × 40	5	7903	60
G6	60 × 40	0	12 403	60

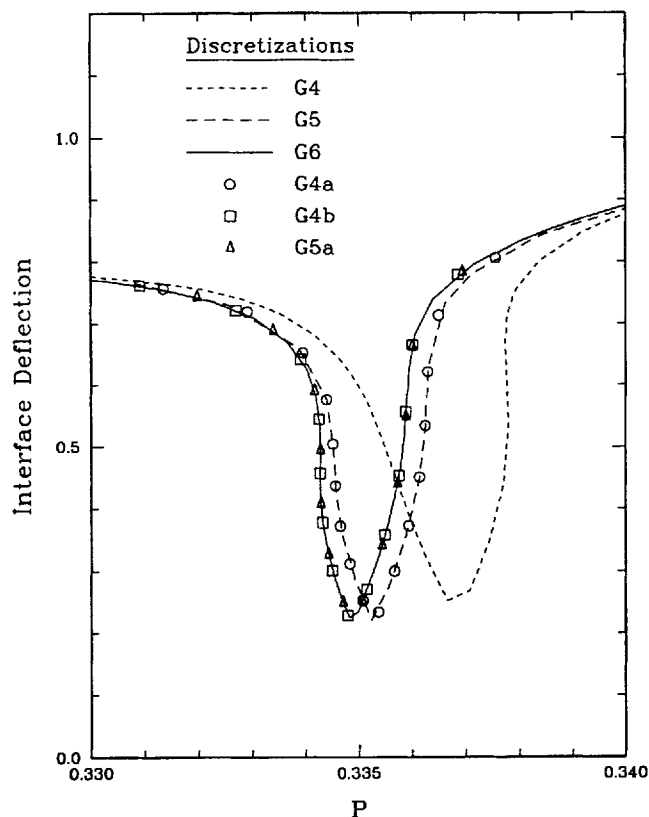
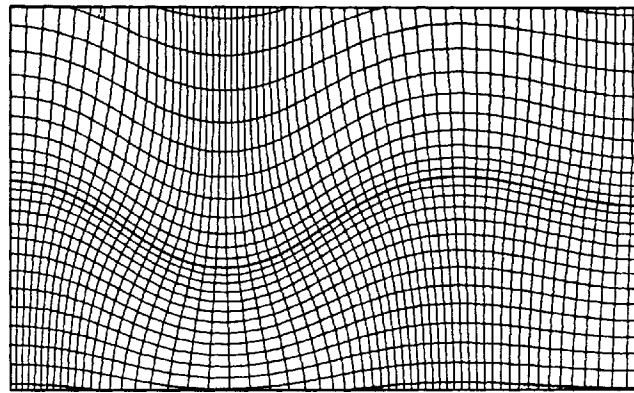


Figure 11. Secondary bifurcation branch for various discretizations. The grids used are explained in Table II

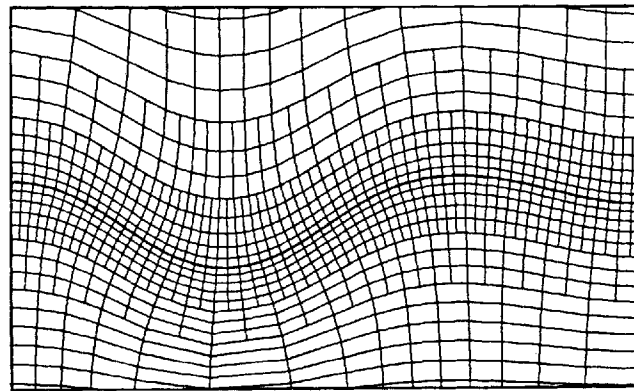
knowns determines the accuracy of the solution. Thus, for a given accuracy, local refinement results in considerable computational savings. An example of a locally refined grid for this case is shown in Figure 12 together with a uniform grid with the same degrees of freedom along the interface.

5. SUMMARY

The calculations presented here show that local refinement around free surfaces is a powerful approach for increasing the accuracy of the solution of free-boundary problems without a signifi-



(a)



(b)

Figure 12. Local mesh refinement near a shallow melt/solid interface: (a) uniform grid G6; (b) locally refined grid G4b listed in Table II are shown. The interface is shown as a thicker co-ordinate line.

cant increase of the total number of unknowns. In the problem considered here, local refinement is uniform in the lateral direction so that it can accommodate for the large variety of interface shapes that appear in a given domain as the parameters change. However, for fixed or slightly changing domains, more sophisticated refinement can be incorporated, resulting in near optimal use of computational resources.

Local refinement also can be very important in applications where the boundary conforming mapping is used simply for grid generation in a fixed domain. Usually in such cases, mapping should provide simultaneously for acceptable levels of smoothness, orthogonality and grid concentration,¹⁹ resulting in very strict requirements to the mapping equations. An alternative to this traditional approach is to first account only for smoothness and orthogonality using some set of mapping equations and then impose any grid concentration requirements through local refinement of the resulting conforming grid. This approach relaxes the requirements on the mapping equations and adds more flexibility to the handling of the three important characteristics of the grid, i.e. smoothness, orthogonality and grid concentration.

ACKNOWLEDGEMENTS

This research was supported by the Microgravity Sciences and Applications Program of the National Aeronautics and Space Administration (NASA) and by the Defense Advanced Research Project Agency (DARPA) of the Department of Defense.

REFERENCES

1. G. Ryskin and L. G. Leal, 'Numerical solution of free-boundary problems in fluid mechanics. Part 1. The finite-difference technique', *J. Fluid Mech.*, **148**, 1–17 (1984).
2. S. F. Kistler and L. E. Scriven, 'Coating flows', in J.R.A. Pearson and S. M. Richardson (eds), *Computational Analysis of Polymer Processing*, Applied Science Publishers, Essex, (1983), pp. 243–299.
3. H. M. Ettouney and R. A. Brown, 'Finite-element methods for steady solidification problems', *J. Comput. Phys.*, **49**, 118–150 (1983).
4. L. H. Ungar, and R. A. Brown, 'Cellular interface morphologies in directional solidification. The one sided model', *Phys. Rev. B*, **30**, 1367–1380 (1984).
5. K. Tsiveriotis and R. A. Brown, 'Boundary conforming mapping applied to highly deformed solidification interfaces', *Int. j. numer. methods fluids*, **14**, 981–1003 (1992).
6. C. Chinnaswamy, B. Amadei and T. H. Illangasekare, 'A new method for finite element transitional mesh generation', *Int. j. numer. methods eng.*, **31**, 1253–1270 (1991).
7. A. K. Gupta, 'A finite element for transition from a fine to a coarse grid', *Int. j. numer. methods. eng.*, **12**, 35–45 (1978).
8. D. P. Young, R. G. Melvin, M. B. Bieterman, F. T. Johnson, S. S. Samant and J. E. Bussolletti, 'A locally refined rectangular grid finite element method: application to computational fluid dynamics and computational physics', *J. Comput. Phys.*, **92**, 1–66 (1991).
9. B. Perry, P. Bar-Yoseph and G. Rosenhouse, 'Towards adaptive mesh refinement: application of new rectangular hybrid finite elements in 2D elasticity problems', *Int. j. numer. methods. eng.*, **30**, 473–489 (1990).
10. G. F. Carey and J. T. Oden, *Finite Elements*, Vol. I, Prentice-Hall, Englewood Cliffs, NJ, 1981.
11. B. M. Irons and A. Razzque, 'Experience with the patch test for convergence of finite elements' in A. K. Aziz (ed.), *The Mathematical Foundations of the Finite Element Method with Applications to Partial Differential Equations*, Academic Press, New York, 1972, pp. 557–587.
12. G. Strang, 'Variational crimes in the finite element method', in A. K. Aziz, (ed.), *The Mathematical Foundations of the Finite Element Method with Applications to Partial Differential Equations*, Academic Press, New York, 1972, pp. 557–587.
13. F. Stummel, 'The limitations of the patch test', *Int. j. numer. methods eng.*, **15**, 177–188 (1980).
14. I. Babuska, J. T. Oden and J. K. Lee, 'Mixed-Hybrid finite element approximations of second-order elliptic boundary-value problems', *Comput. methods appl. mech. eng.*, **11**, 175–206 (1977).
15. M. Reggio, J. Y. Trepanier and R. Camarero, 'A composite grid approach for the Euler equations', *Int. j. numer. methods fluids*, **10**, 161–178 (1990).
16. W. A. Tiller, K. A. Jackson, J. W. Rutter and B. Chalmers, 'The redistribution of solute atoms during the solidification of metals', *Acta Metall.*, **1**, 428–437 (1953).
17. W. W. Mullins and R. F. Sekerka, 'Stability of a planar interface during solidification of a dilute binary alloy', *J. Appl. Phys.*, **35**, 444–451 (1964).
18. N. E. Gibbs, W. G. Poole and P. K. Stockmeyer, 'An algorithm for reducing the bandwidth and profile of a sparse matrix', *SIAM J. Numer. Anal.*, **13**, 236–250 (1976).
19. J. F. Thompson, Z. U. A. Warsi and C. W. Mastin, *Numerical Grid Generation*, North Holland, Amsterdam, 1985.